ROYAL SOCIETY
OF CHEMISTRY

PAPER

Check for updates

Hydrogen defects in LaBi$_2$O$_4$X (X = Cl, Br, and I) Sillén oxyhalide phases and their impacts on ionic transport

ShinYoung Kang, [a] Andrew J. E. Rowberg, [a] Shenli Zhang [ab] and Joel B. Varley *[a]

Sillén oxyhalides have recently emerged as promising materials for both photocatalytic and ionic transport applications, yet the role of likely-ubiquitous hydrogen-related defects in these layered compounds remains largely unexplored. Here, we employ first-principles defect calculations to investigate incorporation energetics for hydrogen- and oxygen-related defects, as well as their migration barriers in LaBi$_2$O$_4$X (X = Cl, Br, I) phases. We find that hydrogen interstitials, particularly protonic species (H$_i^+$), are readily accommodated within the open Bi−O layers. Protons compete with oxygen vacancy donors (V$_O^{2+}$) and charge-compensate with oxygen interstitial acceptors (O$_i^{2-}$). By linking hydrogen defect formation to water- and oxygen-related redox equilibria, we reveal that V$_O^{2+}$ facilitates H$_i^+$ incorporation, while O$_i^{2-}$ promotes interstitial hydroxide formation, establishing a direct connection between proton and oxide-ion transport. Calculated migration barriers indicate that ionic diffusion is confined to Bi−O layers with low barriers of 0.20−0.25 eV for H$_i^+$ and 0.14−0.25 eV for V$_O^{2+}$, suggesting that the materials contain intrinsic pathways for mixed ionic conduction. These results provide a microscopic picture of hydrogen behavior in Sillén oxyhalides and point to design strategies for integrating protonic and oxide-ion transport in layered oxyhalide electrolytes. Band-edge alignment analysis shows that LaBi$_2$O$_4$I provides the optimal combination of hydrogen solubility, oxygen defect stability, and mixed ionic conductivity, highlighting its potential for low-temperature electrochemical and energy-conversion applications. Overall, this work establishes the defect-driven origin of hydrogen transport in Sillén oxyhalides and expands their applicability beyond photocatalysis to mixed ionic conduction and hydrogen electrochemistry.

Introduction

Sillén–Aurivillius compounds are layered materials consisting of alternating fluorite-like [M$_2$O$_2$]$^{2+}$ slabs with perovskite-like or halide interlayers.[1] This structural motif allows versatile chemical modification that can easily tune the electronic and optical properties, as well as flexible morphological regulations with variable number of interlayers during synthesis. Such tunability has highlighted Sillén–Aurivillius compounds as promising and versatile platforms for visible-light photo-catalysts in water splitting.[2–9] Among these, LaBi$_2$O$_4$Cl has been identified as a novel variant of the Sillén phases, containing triple fluorite-like slabs ([M$_3$O$_4$]$^+$) charge-balanced by halide layers.[10] While various Sillén compounds have been recognized for photocatalytic activity like Sillén–Aurivillius phases,[11–13]

Materials Science Division and Laboratory for Energy Application for the Future (LEAF), Lawrence Livermore National Laboratory, Livermore, California 94550, USA. E-mail: varley2@llnl.gov

Department of Chemical and Materials Engineering, San José State University, San Jose, California 95192, USA

LaBi$_2$O$_4$Cl-based oxychloride families have also emerged as fast oxygen-ion conductors: Yaguchi *et al.* demonstrated interstitialcy-driven oxygen transport, reporting conductivities of 10 mS cm^{-1} at 431 °C in Bi$_{1.9}$Te$_{0.1}$LuO$_{4.05}$Cl and 20 mS cm^{-1} at 702 °C in LaBi$_{1.9}$Te$_{0.1}$O$_{4.05}$Cl[14,15]—values that surpass state-of-the-art electrolytes such as yttria-stabilized zirconia (YSZ) and La$_{0.8}$Sr$_{0.2}$Ga$_{0.83}$Mg$_{0.17}$O$_{2.815}$ (LSGM). The corresponding activation energies of 0.22–0.50 eV underline their excellent ionic transport properties. More recently, Meng *et al.* reported exceptionally fast vacancy-mediated oxygen conduction with a migration barrier as low as 0.1 eV.[16]

Beyond their outstanding photocatalytic reactivity and oxygen conductivity, Sillén and Sillén–Aurivillius phases are also considered chemically stable in water. In many Sillén and Sillén–Aurivillius oxyhalides, the valence band edge (VBM) is dominated by oxygen 2p orbitals, which may effectively suppress the self-oxidation of halogen species, *i.e.*, dissolution or volatilization in aqueous environments.[5,13] This raises a critical and largely unexplored question: how do these compounds interact with water, and how do hydrogen-related point defects impact ionic transport?

Compared to established proton- and mixed-conducting oxides such as perovskites (*e.g.*, $BaZrO_3$, $BaCeO_3$) or fluorites, Sillén-type oxyhalides offer a fundamentally distinct structural platform for hydrogen incorporation. Their layered architecture comprises open Bi–O planes separated by halide layers, creating low-coordination environments that possibly affect both the stability and diffusion barriers of hydrogen-related defects. Furthermore, the favorable permeability of oxygen species in Sillén oxyhalides[14-16] suggests defect chemistries that naturally couple proton and oxide-ion transport with strong implications for understanding mixed ion conduction.

The ability of a material to function as an electrolyte or membrane for water-splitting and/or separation-related applications is largely dictated by its chemical stability in water/steam and the permeability of hydrogen defects. Collectively, these factors determine whether these families of compounds could serve as oxygen- or proton-conducting materials for electrochemical devices such as electrolyzer cells, fuel cells, and solid-state separation membranes, provided they satisfy other application-specific properties like controllable electronic conductivity and thermal stability.[17-19] In this work, we use $LaBi_2O_4X$ (X = Cl, Br, or I) oxyhalides as a case study for understanding the consequences of hydrogen incorporation, particularly in the context of ionic transport. Having already demonstrated excellent oxygen conduction in the case of $LaBi_2O_4Cl$, they provide an ideal model to investigate how chemistry influences water-material interactions and whether hydrogen-related defects can be stabilized and mobilized alongside oxygen defects. In this class of materials, halogen substitution provides an effective means of tuning the electronic structure, particularly the band gap and the relative energetics of the band edges. The VBM, which is mainly contributed by oxygen 2p orbitals, is sensitive to the interlayer spacing, itself governed by the choice of halogen species.[2,5,13] Consequently, the coupled structural and electronic modifications induced by halogen substitution can have a profound impact on defect stability and migration kinetics. This study thus bridges the known oxygen-ion conduction with the unexplored potential of protonic transport, expanding the possible application space of Sillén-type oxyhalides beyond photocatalysis into electrochemical energy conversion.

Results and discussions

To assess the relative stability of hydrogen-involving defects in $LaBi_2O_4X$ (X = Cl, Br, and I), we calculated the formation energies for a range of species: interstitials (H_i, O_i, and OH_i), substituted species (H_O and H_X), and vacancies, including those coupled with hydrogen (V_O, V_X, H_i–V_O, H_i–V_X, and H_O–V_O). To calculate the defect formation energies, we adopt the conventional defect supercell approach[20] and use the PBE exchange correlation functional, along with band edge corrections obtained with the HSE06 hybrid functional with spin–orbit corrections,[21,22] as implemented in the VASP code.[23] Additional tests to assess the relevance of charge localization for particular defects and charge states (*e.g.*, V_O^0 and V_O^{2+}, H_i^0, H_i^+, and Bi^{5+} bipolarons) were performed with hybrid functionals and

verified the qualitative defect behavior obtained with PBE. Oxygen- and halogen-rich environments were used for the choice of chemical potentials (see the SI for details). We evaluated three possible interstitial sites: within the La layer, within the halogen (X) layer, and within the Bi_2O_2 layer (Fig. 1(a)). Across all halide variants (X = Cl, Br, I), interstitial acceptors, such as H_i^-, O_i^{2-}, and OH_i^-, are most stable when located near La cations, while the H_i^+ interstitial donor preferentially resides within the Bi–O layer to bond with oxygen anions. Representative lowest-energy configurations are illustrated in Fig. 1(b).

The thermodynamic stability of defects is examined through the defect formation energies, E^f, plotted as a function of the Fermi energy in $LaBi_2O_4Cl$, $LaBi_2O_4Br$, and $LaBi_2O_4I$ (Fig. 2). Note that chemical potentials of O, H, and X are chosen to reflect equilibrium with O_2 gas, H_2O gas, and solid La_2O_3 and Bi_2O_3 phases, consistent with synthesis conditions and those typical of low-temperature water-containing environments (See SI). In all three compounds, V_O^{2+}, H_i^+, and O_i^{2-} emerged as the most stable defects for Fermi levels spanning the band gaps; we indicate transitions between the most favorable defect species with black and yellow stars in Fig. 2. Specifically, V_O^{2+} dominates near the VBM, H_i^+ is preferred at intermediate Fermi levels, and O_i^{2-} becomes most favorable near the conduction band minimum (CBM). Note that, however, the Fermi level regime where V_O^{2+} is dominant over H_i^+ is where $E^f[V_O^{2+}]$ is negative, indicating that these oxyhalides are unstable in these conditions. Neutral O_i^0 is more stable when paired with a lattice oxygen ion to form a dumbbell configuration, $O_i^0(db)$, than as an isolated O_i^0. However, $O_i^{2-}(db)$ is never stabilized relative to either $O_i^0(db)$ or O_i^0 within the band gap for any of the compounds studied. In $LaBi_2O_4I$, we observe that the formation energy of V_I^+ is comparable to that of H_i^+, and thus V_I^+ and H_i^+ will compete as the dominant donor defects. For all compounds, V_O exclusively acts as a double donor for all Fermi levels within their band gaps, which was verified with independent hybrid functional calculations (see Fig. S5). For $LaBi_2O_4Cl$, $E^f[V_O^{2+}]$ at the VBM is −1.71 eV, significantly lower than previously reported values,[16] likely due to differences in correction schemes. For example, the modified band alignment (MBA)[24] used in ref. 16 relies on the neutral state of the defect, which is ill-defined in these materials due to neutral V_O spuriously populating the conduction band with electrons when calculated using PBE, which likely impacts the alignment corrections scheme used in this case. The range of Fermi levels where H_i^+ is the most stable defect decreases from $LaBi_2O_4Cl$, $LaBi_2O_4Br$, to $LaBi_2O_4I$, which we later discuss in the context of relative band alignments. We give approximate Fermi-level positions expected from charge-neutrality for these defects, which is governed by the crossing of the H_i^+ and O_i^{2-} defects; these Fermi levels are denoted by yellow stars in Fig. 2. Note that in its ground-state configuration, the H_i^+ defect forms a localized protonic species by binding to an oxygen atom in the Bi–O layer, with a relaxed O–H bond length of approximately 0.99 Å and no significant hydrogen bonding to neighboring oxygen atoms in all $LaBi_2O_4X$ compounds. Moreover, proton decoration of the $O_i^{2-}(db)$ configuration leads to spontaneous relaxation toward the interstitial hydroxide species, OH_i^-, coupled with
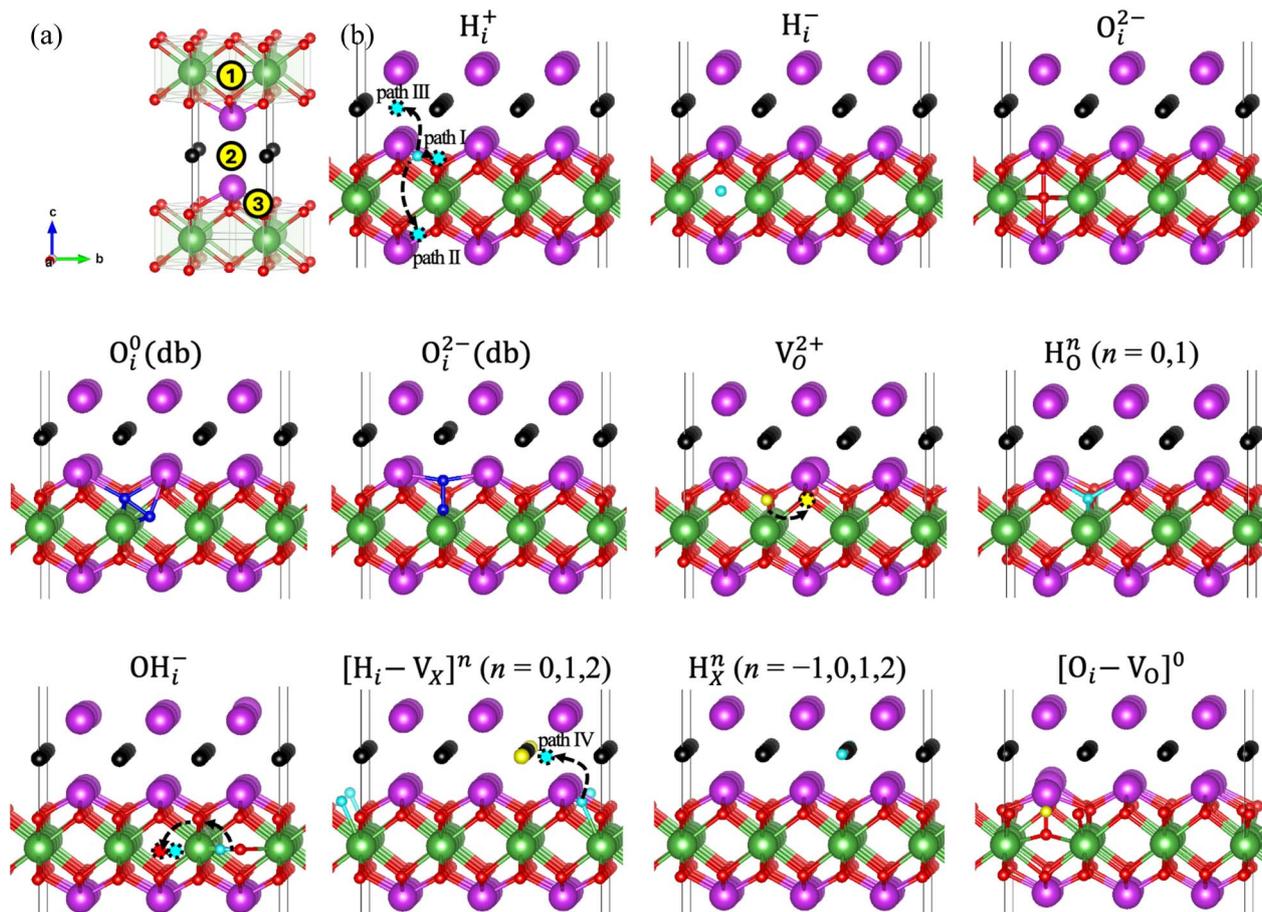
Fig. 1 (a) Unit cell structure of $LaBi_2O_4X$ (X = Cl, Br, or I) with denoted candidate interstitial sites. (b) Lowest energy configurations and diffusion pathways for a few selected defects considered in this study. Green, purple, red, black, and cyan spheres represent La, Bi, O, X, and H atoms. Yellow spheres depict vacancies. O_i^0(db) and O_i^{2-}(db) denote an oxygen interstitial paired with a lattice oxygen ion to form a dumbbell configuration. The oxygen pairs are indicated as blue spheres.

a lattice oxygen, reinforcing that hydrogen–oxygen defect interactions are more likely to manifest as hydroxide formation.

By contrast, defect complexes involving trapping of hydrogen defects in halogen or oxygen vacancies (H_O and H_X) are consistently high in energy (>2 eV), suggesting they are rare, at least under the considered conditions. We found that the H_i–V_O complex recombines into H_O in all compounds. Hydride ions, H_i^-, in the La layer are also less stable than protons, H_i^+, on the

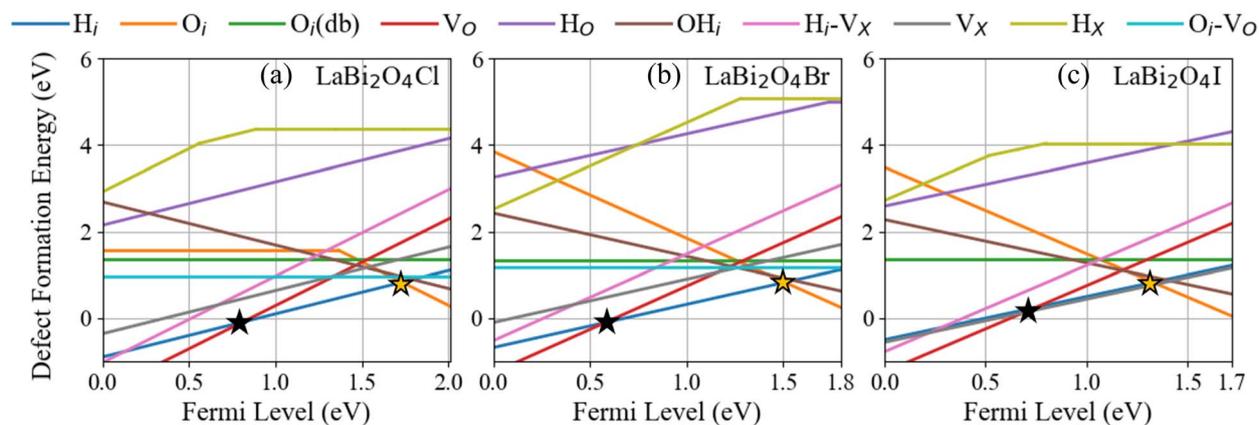**Fig. 2** Defect formation energies, E^f, calculated in (a) $LaBi_2O_4Cl$, (b) $LaBi_2O_4Br$, and (c) $LaBi_2O_4I$ computed at oxygen- and halogen-rich conditions. The VBM level is set to zero in each material. Black and yellow stars represent the Fermi level positions where $E^f[H_i^+] = E^f[V_O^{2+}]$ and $E^f[H_i^+] = E^f[O_i^{2-}]$, respectively.

Bi_2O_2 layer by 6.0, 5.6, and 5.2 eV in –Cl, –Br, and –I compounds, respectively. In addition, we found that the interstitial hydroxide species, OH_i^-, essentially a complex between O_i^{2-} and H_i^+, has meaningful stability, especially for n-type conditions, with $E^f[OH_i^-] = 0.93$, 0.88, and 0.77 at the CBM for –Cl, –Br, and –I compounds, respectively. These results indicate that $LaBi_2O_4X$ readily accommodates H_i^+, O_i^{2-}, and OH_i^-, consistent with the open structure of the Sillén phases.

The calculated E^f values further inform the reaction thermodynamics for proton formation. Table 1 summarizes three representative processes: (1) water-splitting (and proton-incorporation) aided by V_O^{2+}, (2) direct water-splitting into H_i^+ and OH_i^-, and (3) proton-liberation from reactions between V_O^{2+} and OH_i^-. Note that these reaction energies are independent of the choice of element chemical potentials. The proton formation aided by V_O^{2+} is an exothermic reaction for $LaBi_2O_4Cl$ but becomes less favorable in the –I analog (from −0.09 to 0.24 eV/H_i^+ for –Cl and –I compounds). On the other hand, despite the low E^f of OH_i^- (<1 eV at the CBM), direct formation of $H_i^+ + OH_i^-$ from water is energetically prohibitive (>1.70 eV/H_i^+) for all compounds. However, OH_i^- can react with V_O^{2+} to form protons with low reaction energies from −1.88 to −1.34 eV/H_i^+. It is worth noting that these calculated proton formation energies are valid only in the bulk. In other words, surface reactions and materials conditions—such as microstructure—significantly impact the defect formation energies, and hence reaction energetics, summarized here. Hydrogen incorporation from water is inherently a surface-mediated process involving adsorption and dissociation steps, which are not explicitly treated in this work. However, given the layered topology and open Bi–O planes of Sillén-type oxyhalides, bulk defect energetics provide a meaningful first-order description of hydrogen stability and transport once incorporation occurs. These results highlight the importance of oxygen defects as mediators for hydrogen incorporation, as the V_O^{2+}-aided water-splitting reaction is the most kinetically preferred route to generate H_i^+, with $LaBi_2O_4Cl$ providing the most favorable environment. The overall contributions of the reaction to proton solubility need more systematic studies that consider structural inhomogeneity, along with processing conditions.

To characterize hydrogen trapping at defects, the binding energies of hydrogen defects, H_i^+ and H_i^-, with low-energy oxygen defects, O_i^{2-} and V_O^{2+}, are evaluated (Table 1). By convention, a negative binding energy indicates attraction and thus promotes hydrogen trapping at that site. Two reactions are consistently favorable across all halides: (i) a proton binding with an oxygen interstitial to form an interstitial hydroxide (reaction 4), and (ii) a hydride binding with an oxygen vacancy to form a substitutional H_O^+ defect (reaction 5). Combining reactions 1, 3, and 4 with the formation energies in Fig. 2, one can identify the optimal conditions to increase proton solubility in these materials. For example, shifting the Fermi level closer to the CBM (e.g. via donor doping) will stabilize oxygen interstitials over vacancies, consuming protons to form hydroxides (reaction 4) and thereby reducing bulk proton solubility. When the Fermi level is closer to the VBM (e.g. via acceptor doping), on the other hand, oxygen vacancies become dominant and promote the formation of protons (reaction 3). Both reactions are expected to influence oxygen conductivity by altering the relative concentrations of O_i^{2-}, V_O^{2+}, and OH_i^-. Both V_O^{2+} and O_i^{2-} have been identified as primary carriers for oxygen diffusion in Sillén phases.[14–16]

Despite favorable reaction energies, we note that reactions 5 and 6 (involving hydride ions) are not expected to be relevant, since H_i^- are never predicted to be favored over H_i^+ (Fig. 2). Similarly, proton trapping in a halide ion vacancy, V_X^+, (reaction 9) is thermodynamically highly unfavorable with low reaction rates attributed to the high $E^f[H_X^{2+}]$, while protons can easily bind with V_X^+ (reaction 8). The impact of V_X^+ on proton migration kinetics will be discussed in the following section. Additionally, we find that annihilation of V_O^{2+} and O_i^{2-} is substantially more favorable than Frenkel pair formation in all three oxyhalide systems, suggesting the importance of stoichiometry control and operation conditions for achieving high oxide conductivity.

To compare defect energetics and redox potentials across compounds, VBMs and CBMs of Sillén phases are aligned to the vacuum level using surface models (Fig. 3(a)). Additional details on the band-alignment procedure, including a comparison with bulk core-level alignment, are provided in the SI. Interestingly,

Table 1 Calculated reaction energies in bulk for proton formation and trapping, and oxygen defect annihilation

Reaction	Reaction energies		X = Cl	X = Br	X = I
Proton formation (eV/H_i^+)	(1) $V_O^{2+} + H_2O \rightarrow 2H_i^+$		−0.09	−0.10	0.24
	(2) $H_2O \rightarrow H_i^+ + OH_i^-$		1.78	1.85	1.86
	(3) $V_O^{2+} + OH_i^- \rightarrow H_i^+$		−1.88	−1.76	−1.34
Hydrogen defect trapping (eV/H_i)	(4) $H_i^+ + O_i^{2-} \rightarrow OH_i^-$		−0.71	−0.84	−0.90
	(5) $H_i^- + V_O^{2+} \rightarrow H_O^+$		−1.25	−0.38	−0.90
	(6) $H_i^+ + V_O^0 \rightarrow H_O^+$		−0.07	0.64	−0.55
	(7) $H_i^+ + V_O^{2+} + e^- \rightarrow H_O^+ + h^+$	at VBM	4.77	5.10	4.21
		at CBM	0.74	1.51	0.77
	(8) $H_i^+ + V_X^+ \rightarrow [H_i - V_X]^{2+}$		0.24	0.16	0.15
	(9) $H_i^+ + V_X^+ \rightarrow H_X^{2+}$		4.19	3.20	3.65
Oxygen defect annihilation (eV/O)	(10) $V_O^{2+} + O_i^{2-} \rightarrow O_O^0$		−2.59	−2.60	−2.24
Oxygen frenkel pair formation energy (eV/O)	(11) $V_O^{2+} + O_i^{2-} \rightarrow V_O^{2+} - O_i^{2-}$		−1.61[a]	−1.41[a]	N/A[b]

[a] To avoid O_i^{2-} migration to V_O^{2+} and annihilation, the position of O_i^{2-} was fixed. [b] The $V_O^{2+} - O_i^{2-}$ configuration could not be stabilized in $LaBi_2O_4I$.
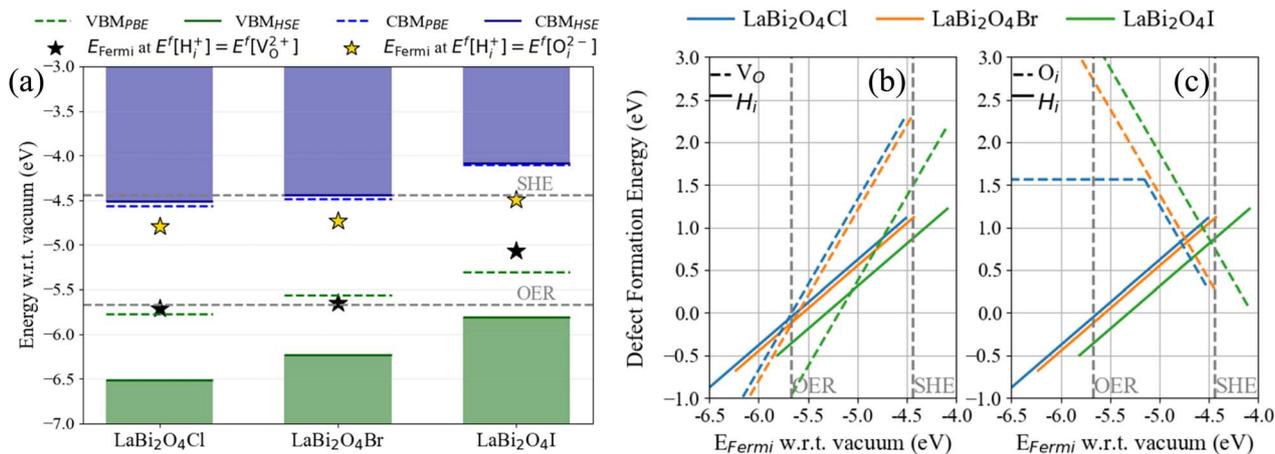
Fig. 3 (a) Variation of energy levels in LaBi$_2$O$_4$Cl, LaBi$_2$O$_4$Br, and LaBi$_2$O$_4$I, showing VBMs (horizontal green lines) and CBMs (horizontal blue lines) calculated using PBE (dashed lines) and HSE06 (solid lines) functionals. Yellow star markers represent the Fermi levels when the formation energy of proton interstitials donors, H$_i^+$, equals that of O$_i^{2-}$ acceptors for our studied conditions, as in Fig. 2. Black star markers are for the equilibrium between H$_i^+$ and V$_O^{2+}$ donors. Formation energies of H$_i^+$ compared to (b) V$_O$ and (c) O$_i$. The vacuum level is set to zero in the y-axis of (a) and x-axis of (b and c). Gray dashed lines indicate the standard hydrogen electrode (SHE) and the oxygen evolution reaction (OER) potentials, which are −4.44 and −5.67 eV with respect to vacuum, respectively.

the PBE and HSE06 functionals yielded consistent CBM positions for the same lattice constants, while HSE06 shifted the VBMs downward with respect to those from PBE, resulting in the band gap widening from 1.21 to 2.01 eV (X = Cl), from 1.08 to 1.80 eV (X = Br), and from 1.21 to 1.72 eV (X = I). The corresponding ionization potentials are 5.77, 5.56, and 5.31 eV in PBE, and 6.52, 6.23, and 5.81 eV in HSE06 for the –Cl, –Br, and –I phases, respectively. From these energies, we can directly compare the relative and absolute band edge positions across these materials, enabling predictions of charge transfer, interface behavior, and band alignments. For (photo)catalytic applications, this is useful for understanding how the band edges straddle important redox potentials; for instance, having the CBM above the standard hydrogen electrode (SHE) potential (0 V $vs.$ SHE) can facilitate reductive electron transfer for the hydrogen evolution reaction (HER), and/or a VBM below the oxygen evolution reaction (OER) potential (+1.23 V $vs.$ SHE) can facilitate oxidative hole transfer. For this particular example, this translates to electron affinities closer to the vacuum level than the SHE potential (−4.44 eV)[25] and ionization potentials further away than the OER potential (−5.67 eV). Our band alignment in Fig. 3(a) shows that all VBMs computed in the HSE06 functional are positioned below the OER level, while only LaBi$_2$O$_4$I has a CBM positioned above the HER level. Interestingly, the BiOX (X = Cl, Br, I) family, whose layered structure consists of alternating [Bi$_2$O$_2$]$^{2+}$ slabs and double halogen layers analogous to those in Sillén phases, has demonstrated promising photocatalytic activity owing to their well-aligned band edge positions.[26,27]

Overall, the defect formation energies suggest that H$_i^+$ and V$_O^{2+}$ are the competing dominant hydrogen and oxygen defects at E_{Fermi} closer to the VBM, while H$_i^+$ and O$_i^{2-}$ (and V$_I^+$ in LaBi$_2$O$_4$I) are dominant at E_{Fermi} closer to the CBM. Assuming these water-related defects are the dominant charged species, which follows from their low formation energies in Fig. 2,

charge neutrality should be determined by compensation between H$_i^+$ and O$_i^{2-}$ (and V$_I^+$ in LaBi$_2$O$_4$I), leading to Fermi levels in the vicinity of the yellow stars in Fig. 2 and 3. This Fermi level value falls within the band gap for all of the studied oxyhalides but is close to the CBM, suggesting water-related defects may have larger indirect effects on ionic conduction by suppressing the concentrations of mobile V$_O^{2+}$ rather than strongly impacting the electronic conductivity. We note that this simple analysis does not account for other impurity or dopant effects that could shift the Fermi level if concentrations are comparable to those of the hydrogen- or oxygen-related defects.

To gain insight into the relative proton solubility in the oxyhalides at a common electrochemical reference, we replotted the defect formation energies as a function of Fermi level referenced to vacuum in Fig. 3(b and c). These results highlight how, for the same conditions, the proton formation energy in LaBi$_2$O$_4$I is 0.17 (0.21 eV) lower than that in LaBi$_2$O$_4$Cl (LaBi$_2$O$_4$Br). Interestingly, V$_O^{2+}$ formation is also more favorable in LaBi$_2$O$_4$I by 0.95 (0.84 eV) than in LaBi$_2$O$_4$Cl (LaBi$_2$O$_4$Br), suggesting that LaBi$_2$O$_4$I can incorporate much higher concentrations of H$_i^+$ and V$_O^{2+}$ than the other two under identical conditions. On the other hand, the formation energy of O$_i^{2-}$ in LaBi$_2$O$_4$I is 0.61 (0.48 eV) higher than that in LaBi$_2$O$_4$Cl (LaBi$_2$O$_4$Br). Thus, at common absolute Fermi levels and conditions, the formation energies of O$_i^{2-}$ (V$_O^{2+}$) are positively (negatively) correlated with the halide electronegativity in the LaBi$_2$O$_4$X series, with LaBi$_2$O$_4$I having the lowest $E^f[\text{V}_O^{2+}]$ and highest $E^f[\text{O}_i^{2-}]$, in addition to the lowest $E^f[\text{H}_i^+]$. This suggests that LaBi$_2$O$_4$I is more effective than –Cl and –Br phases at promoting V$_O$ formation and suppressing O$_i$ formation. Considering that V$_O$ is a primary carrier for oxygen conductivity in LaBi$_2$O$_4$Cl, LaBi$_2$O$_4$I would greatly benefit from increasing the solubility of mobile oxygen defects.

Table 2 Migration barriers in eV. Illustration of pathway can be found in Fig. 1. Values in parentheses are the reverse barriers when the initial and final sites are symmetrically distinct

Species	Migration pathways	X = Cl	X = Br	X = I
H_i^+	Path I: in-plane on Bi–O layer without V_X	0.24	0.25	0.20
—	Path I′: in-plane on Bi–O layer with V_X	0.15	0.16	0.16
—	Path II: between Bi–O layers	0.78	0.72	0.65
—	Path III: from Bi–O layer to X layer without V_X	1.79 (0.11)	1.95 (0.22)	2.01 (0.44)
—	Path IV: from Bi–O layer to X layer with V_X	2.02 (0.00)	2.19 (0.00)	2.11 (0.00)
OH_i^-	In-plane on La layer	0.87	0.85	0.85
O_i^{2-}	In-plane on La layer	0.81	0.86	0.94
V_O^{2+}	In-plane on Bi–O layer	0.14	0.18	0.25

The overall favorable formation of H_i^+ in these oxyhalides naturally raises the question of whether they are promising candidates as mixed ionic conductors. To address this question, we computed the migration barriers of hydrogen and oxygen defects using the Climbing Image Nudged Elastic Band (CI-NEB) calculations[28] to fully assess their conductivity. Four migration pathways were considered for H_i^+, namely, interlayer and intralayer pathways with and without a halogen vacancy. These pathways are illustrated in Fig. 1(b), and their barriers are summarized in Table 2. Hopping from one lowest-energy Bi–O layer site to another includes two-dimensional (2D) in-plane migration and three-dimensional (3D) out-of-plane migration (Path I and II). The 2D diffusion pathway exhibits low barriers of

0.20–0.25 eV, while 3D diffusion across the La layer shows moderate barriers of 0.65–0.78 eV in all compounds.

These results suggest that these Sillén phases could serve as fast proton conducting materials dominated by 2D conductivity at low temperatures, while the quasi-3D diffusion mechanism could be activated at higher temperatures, thereby fully utilizing the interconnected network of La–O polyhedra. Interestingly, the migration barriers show little variation across the halide series, despite the increase in the lattice constants and the hopping distances from –Cl to –I. Due to the high site energy on the halogen layer, migration barriers there are higher than 1.7 eV (Path III), inhibiting the full 3D diffusion beyond the Bi–O layer. We confirmed that halogen vacancies do not help access the full 3D diffusion (Path IV). However, notably, halogen
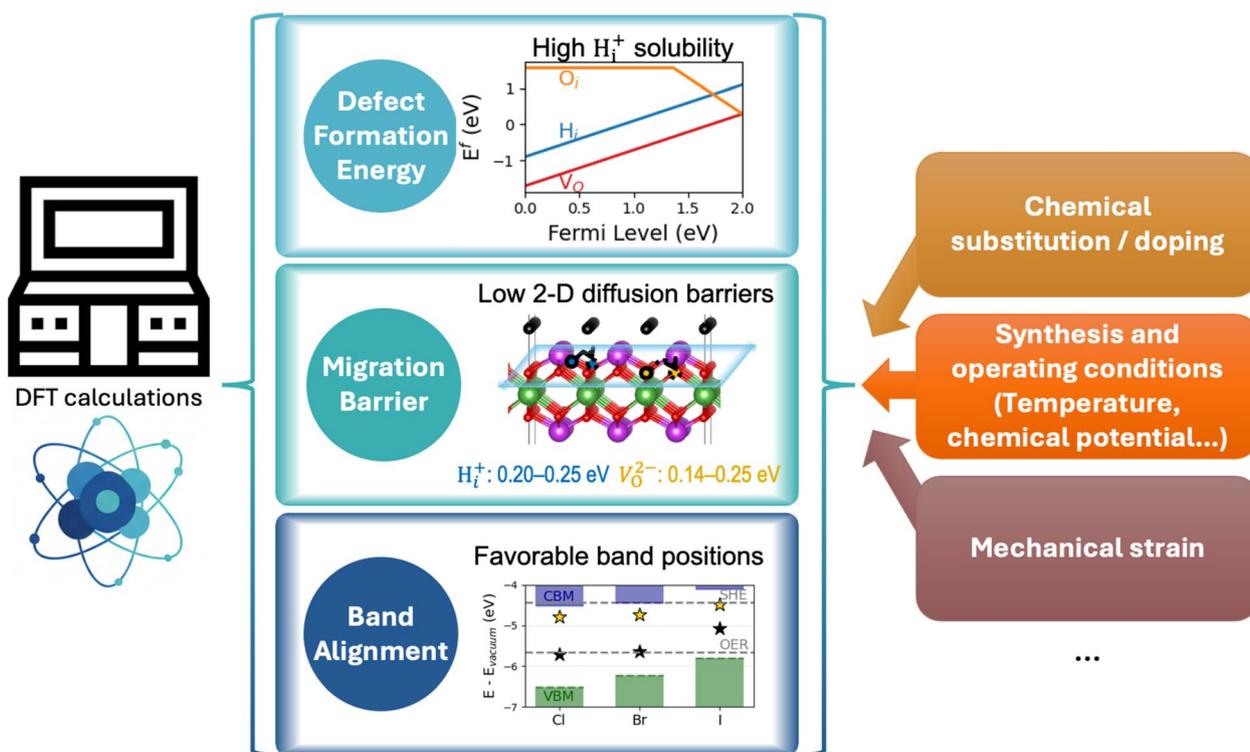

Fig. 4 Schematic of DFT-predicted properties for $LaBi_2O_4X$ Sillén phases, including high proton solubility, its low 2-D diffusion barriers, and favorable band edge positions. These results provide an outlook for further optimization *via* chemical substitution/doping, environmental conditions, strain, and so on.

vacancies can further accelerate the 2D conductivity by lowering the Bi–O in-plane migration barriers by 0.04–0.09 eV (Path I'). We found that the V_X^+ induces slight structural distortions on the adjacent Bi–O plane, leading to lower the H migration barrier. Considering the sensitive stability competition between H_i^+ and V_X^+, especially in LaBi$_2$O$_4$I (Fig. 2), the beneficial impact of V_X^+ on hydrogen transport is encouraging.

As H_i^+ easily reacts with O_i^{2-} to form OH_i^- (reaction 3 in Table 1), we also computed the migration barriers of OH_i^-. The barriers range from 0.85–0.87 eV and can be activated at high temperatures. The migration barriers of O_i^{2-} and V_O^{2+} are 0.81–0.94 eV and 0.14–0.25 eV, respectively, in good agreement with recent reports.[16] In contrast to H_i^+, the migration barriers of OH_i^-, O_i^{2-}, and V_O^{2+} do show a stronger dependence on the halide, increasing from –Cl to –I. We attribute this to the stronger Bi–O bond in materials with smaller lattice constants, which aids the migration of oxygen-related defects by reducing their hopping distance, while more rigid Bi–O bonds may hinder the rotation of O–H bonds and proton hopping.

Overall, these results establish that LaBi$_2$O$_4$X Sillén phases can host both oxygen and hydrogen defects, with distinct trends across halide chemistry. LaBi$_2$O$_4$Cl shows the most favorable oxygen vacancy-assisted proton generation, while LaBi$_2$O$_4$I combines favorable proton transport with enhanced defect solubility for both hydrogen and oxygen, making it a promising candidate for mixed ionic conduction. Both LaBi$_2$O$_4$Cl and LaBi$_2$O$_4$I are reported to be thermodynamically stable within the quaternary La–Bi–O–X phase diagrams,[29] and their successful synthesis has been experimentally demonstrated.[10,16,30] Interestingly, LaBi$_2$O$_4$I has been theoretically predicted to exhibit promising optoelectronic and thermoelectric performance, attributed to its strong optical response in the visible–ultraviolet range and favorable band topology.[31] Taken together, these results suggest that LaBi$_2$O$_4$I offers an attractive combination of bulk hydrogen solubility, transport properties, and intrinsic stability, while recognizing that the optimal halogen composition under realistic operating conditions will depend on surface insertion kinetics and chemical stability. More broadly, this work delineates a clear design space in which halogen chemistry can be leveraged to balance hydrogen incorporation and transport for targeted electrochemical applications as summarized in Fig. 4.

Conclusions

In summary, we have described water-related defects in LaBi$_2$O$_4$X (X = Cl, Br, I) Sillén phases. Our first-principles defect calculations reveal that these materials can readily incorporate hydrogen defects, with proton solubility inversely proportional to the halide size/electronegativity at common electrochemical reference energies. Protons have low migration barriers (0.20–0.25 eV) along the Bi–O layers that enable facile 2D conductivity, with barriers largely independent of the halide species. While oxygen vacancy-assisted water splitting is the most plausible route for proton generation, oxygen interstitials can also bind with protons to form interstitial hydroxide species. Thus, proton solubility and transport are intimately connected with

water and oxygen atmospheres, and controlled defect engineering will be essential to maximize proton solubility. Notably, while proton transport is largely insensitive to the halide but becomes slightly easier with increasing molar volume from Cl to I, migration of oxygen-related defects shows the opposite trend, with V_O^{2+} migration remaining comparably facile with barriers on the order of 0.14–0.25 eV. These findings suggest that, while all of these LaBi$_2$O$_4$X oxyhalides may serve as mixed ionic conductors, LaBi$_2$O$_4$Cl is most favorable for vacancy-assisted proton generation based on bulk reaction energetics, whereas LaBi$_2$O$_4$I offers a favorable combination of bulk proton solubility and mobility once hydrogen is incorporated. Which halogen composition is preferred will depend on the specific operating regime, including the relative importance of surface incorporation kinetics, environmental conditions, and chemical stability. Further investigations of stability, synthesizability, and electrochemical performance under operating conditions are needed to evaluate this material for ionic transport and photocatalytic applications. Overall, this work expands the potential of Sillén oxyhalides beyond their established photocatalytic applications, highlighting their promise as electrolytes or membranes in low-temperature electrochemical devices.

Conflicts of interest

There are no conflicts to declare.

Data availability

The data supporting this article have been included as part of the supplementary information (SI). Supplementary information: DFT settings, summary of structural and electronic properties of bulk LaBi$_2$O$_4$X, reference chemical potentials, and energy level alignment approaches. See DOI: https://doi.org/10.1039/d5ta09720g.

Acknowledgements

References

1 O. K. Moune-Minn, L. Albert and P. Caro, Synthesis and spectroscopic properties of the sillen phases, *J. Less-Common Met.*, 1983, **93**(1), 143–150, DOI: 10.1016/0022-5088(83)90459-9.

2 J. Chen, Y. Gu, S. Xu, Y. Zhang, Z. Zhang, L. Shi, Z. Mu, C. Zhou, J. Zhang and Q. Zhang, Band Gap Engineering in

Quadruple-Layered Sillén–Aurivillius Perovskite Oxychlorides Bi7Fe2Ti2O17X (X = Cl, Br, I) for Enhanced Photocatalytic Performance, *Catalysts*, 2023, **13**, 751.

3 V. Werner, U. Aschauer, G. J. Redhammer, J. Schoiber, G. A. Zickler and S. Pokrant, Synthesis and Structure of the Double-Layered Sillén–Aurivillius Perovskite Oxychloride La2.1Bi2.9Ti2O11Cl as a Potential Photocatalyst for Stable Visible Light Solar Water Splitting, *Inorg. Chem.*, 2023, **62**(17), 6649–6660, DOI: 10.1021/acs.inorgchem.3c00116.

4 M. Ogawa, H. Suzuki, K. Ogawa, H. Ubukata, O. Tomita, A. Nakada, S. Nozawa, A. Saeki, H. Kageyama and R. Abe, Flux Synthesis of Sillén–Aurivillius Oxyiodide for Visible Light Water Splitting Photocatalysis, *Chem. Mater.*, 2025, **37**(3), 1123–1131, DOI: 10.1021/acs.chemmater.4c02946.

5 K. Ogawa, H. Suzuki, A. Walsh and R. Abe, Orbital Engineering in Sillén–Aurivillius Phase Bismuth Oxyiodide Photocatalysts through Interlayer Interactions, *Chem. Mater.*, 2023, **35**(14), 5532–5540, DOI: 10.1021/acs.chemmater.3c00932.

6 J. Yang, Y. Xue, C. Han, X. Zhang, K. Sa, J. Jia, H. Ye and Y. Liang, In situ construction of a Sillén–Aurivillius layered perovskite-based 0D/2D homologous Schottky junction for efficient piezo-photocatalytic activity, *Catal. Sci. Technol.*, 2023, **13**(18), 5313–5325, DOI: 10.1039/D3CY00876B.

7 D. Ozaki, H. Suzuki, K. Ogawa, R. Sakamoto, Y. Inaguma, K. Nakashima, O. Tomita, H. Kageyama and R. Abe, Synthesis, band structure and photocatalytic properties of Sillén–Aurivillius oxychlorides BaBi5Ti3O14Cl, Ba2Bi5Ti4O17Cl and Ba3Bi5Ti5O20Cl with triple-, quadruple- and quintuple-perovskite layers, *J. Mater. Chem. A*, 2021, **9**(13), 8332–8340, DOI: 10.1039/D0TA12550D.

8 D. Ozaki, H. Suzuki, O. Tomita, Y. Inaguma, K. Nakashima, H. Kageyama and R. Abe, A new lead-free Sillén–Aurivillius oxychloride Bi5SrTi3O14Cl with triple-perovskite layers for photocatalytic water splitting under visible light, *J. Photochem. Photobiol., A*, 2021, **408**, 113095, DOI: 10.1016/j.jphotochem.2020.113095.

9 S. Xu, Y. Zhang, Y. Wang, J. Chen, C. Zhou, Z. Mu, Z. Zhang, J. Zhang, J. Wang and Q. Zhang, Coupled ferroelectric polarization in novelty Sillén–Aurivillius BaBi4TiNbO11Cl material for photocatalysis, *J. Alloys Compd.*, 2023, **952**, 169932, DOI: 10.1016/j.jallcom.2023.169932.

10 C. J. Milne, P. Lightfoot, J. D. Jorgensen and S. Short, Synthesis and structure of Bi2LaO4Cl: a novel variant of the sillen phases, *J. Mater. Chem.*, 1995, **5**(9), 1419–1421, DOI: 10.1039/JM9950501419.

11 W. Dong, T. Xie, Z. Wu, H. Peng, H. Ren, F. Meng and H. Lin, Oxygen-vacancy-rich BiOCl materials with ultrahigh photocatalytic efficiency by etching bismuth glass, *RSC Adv.*, 2021, **11**(61), 38894–38906, DOI: 10.1039/D1RA06961F.

12 Y. Shi, J. Li, C. Mao, S. Liu, X. Wang, X. Liu, S. Zhao, X. Liu, Y. Huang and L. Zhang, Van Der Waals gap-rich BiOCl atomic layers realizing efficient, pure-water CO2-to-CO photocatalysis, *Nat. Commun.*, 2021, **12**(1), 5923, DOI: 10.1038/s41467-021-26219-6.

13 H. Suzuki, H. Kunioku, M. Higashi, O. Tomita, D. Kato, H. Kageyama and R. Abe, Lead Bismuth Oxyhalides PbBiO2X (X = Cl, Br) as Visible-Light-Responsive Photocatalysts for Water Oxidation: Role of Lone-Pair Electrons in Valence Band Engineering, *Chem. Mater.*, 2018, **30**(17), 5862–5869, DOI: 10.1021/acs.chemmater.8b01385.

14 H. Yaguchi, D. Morikawa, T. Saito, K. Tsuda and M. Yashima, High Oxide-Ion Conductivity through the Interstitial Oxygen Site in Sillén Oxychlorides, *Adv. Funct. Mater.*, 2023, **33**(27), 2214082, DOI: 10.1002/adfm.202214082.

15 N. Ueno, H. Yaguchi, K. Fujii and M. Yashima, High Conductivity and Diffusion Mechanism of Oxide Ions in Triple Fluorite-Like Layers of Oxyhalides, *J. Am. Chem. Soc.*, 2024, **146**(16), 11235–11244, DOI: 10.1021/jacs.4c00265.

16 J. Meng, M. S. Sheikh, L. E. Schultz, W. O. Nachlas, J. Liu, M. P. Polak, R. Jacobs and D. Morgan, Ultrafast Oxygen Conduction in Sillén Oxychlorides, *Chem. Mater.*, 2025, **37**(9), 3147–3157, DOI: 10.1021/acs.chemmater.4c03163.

17 A. J. E. Rowberg, M. Li, T. Ogitsu and J. B. Varley, Incorporation of protons and hydroxide species in BaZrO3 and BaCeO3, *Mater. Adv.*, 2023, **4**(23), 6233–6243, DOI: 10.1039/D3MA00308F.

18 A. J. E. Rowberg, M. Li, T. Ogitsu and J. B. Varley, Polarons and electrical leakage in BaZrO_3 and BaCeO_3, *Phys. Rev. Mater.*, 2023, **7**(1), 015402, DOI: 10.1103/PhysRevMaterials.7.015402.

19 S. Zhang, A. J. E. Rowberg, T. Ogitsu, T. A. Pham and J. B. Varley, Electron-Phonon Renormalization in the Proton-Conducting Electrolyte $\mathrm{Ba}\mathrm{Zr}\mathrm{O}_3$ and Its Implications for High-Temperature Electrolysis, *PRX Energy*, 2025, **4**(1), 013013, DOI: 10.1103/PRXEnergy.4.013013.

20 C. Freysoldt, B. Grabowski, T. Hickel, J. Neugebauer, G. Kresse, A. Janotti and C. G. Van de Walle, First-principles calculations for point defects in solids, *Rev. Mod. Phys.*, 2014, **86**(1), 253–305, DOI: 10.1103/RevModPhys.86.253.

21 J. P. Perdew, K. Burke and M. Ernzerhof, Generalized gradient approximation made simple, *Phys. Rev. B:condens. Matter Mater. Phys*, 1996, **77**, 3865, DOI: 10.1103/PhysRevLett.77.3865.

22 A. V. Krukau, O. A. Vydrov, A. F. Izmaylov and G. E. Scuseria, Influence of the exchange screening parameter on the performance of screened hybrid functionals, *J. Chem. Phys.*, 2006, **125**(22), DOI: 10.1063/1.2404663.

23 G. Kresse and D. Joubert, From ultrasoft pseudopotentials to the projector augmented-wave method, *Phys. Rev. B:condens. Matter Mater. Phys*, 1999, **59**(3), 1758–1775, DOI: 10.1103/PhysRevB.59.1758.

24 M. P. Polak, R. Kudrawiec, R. Jacobs, I. Szlufarska and D. Morgan, Modified band alignment method to obtain hybrid functional accuracy from standard DFT: Application to defects in highly mismatched III-V:Bi alloys, *Phys. Rev. Mater.*, 2021, **5**(12), 124601, DOI: 10.1103/PhysRevMaterials.5.124601.

25 S. Trasatti, The absolute electrode potential: an explanatory note (Recommendations 1986), *Pure Appl. Chem.*, 1986, **58**(7), 955–966, DOI: 10.1351/pac198658070955.

26 Z. Ali, J. Ma, M. Hong and R. Sun, Review: applications of the functional photocatalysts BiOX (X = Cl, Br, I) for clean energy, the environment, and future photobiorefineries, *J. Mater. Chem. A*, 2023, **11**(7), 3297–3314, DOI: 10.1039/D2TA09877F.

27 A. Hussain, J. Hou, M. Tahir, S. S. Ali, Z. U. Rehman, M. Bilal, T. Zhang, Q. Dou and X. Wang, Recent advances in BiOX-based photocatalysts to enhanced efficiency for energy and environment applications, *Catal. Rev.*, 2024, **66**(1), 119–173, DOI: 10.1080/01614940.2022.2041836.

28 G. Henkelman, A. Arnaldsson and H. Jonsson, A fast and robust algorithm for Bader decomposition of charge density, *Comput. Mater. Sci.*, 2006, **36**(3), 354–360, DOI: 10.1016/j.commatsci.2005.04.010.

29 A. Jain, S. P. Ong, G. Hautier, W. Chen, W. D. Richards, S. Dacek, S. Cholia, D. Gunter, D. Skinner, G. Ceder, *et al.*, Commentary: The Materials Project: A materials genome approach to accelerating materials innovation, *APL Mater.*, 2013, **1**(1), 011002, DOI: 10.1063/1.4812323.

30 M. Schmidt, H. Oppermann, C. Hennig, R. W. Henn, E. Gmelin, N. Söger and M. Binnewies, Untersuchungen zu Bismutseltenerdoxidhalogeniden der Zusammensetzung Bi2SEO4X (X = Cl, Br, I), *Z. Anorg. Allg. Chem.*, 2000, **626**(1), 125–135, DOI: 10.1002/(SICI)1521-3749(200001)626:1<125::AID-ZAAC125>3.0.CO;2-S.

31 R. K. Joshi, S. R. Bhandari and M. P. Ghimire, Structural stability, electronic, optical, and thermoelectric properties of layered perovskite Bi2LaO4I, *RSC Adv.*, 2022, **12**(37), 24156–24162, DOI: 10.1039/D2RA03859E.